



Enhancement of electrical conductivity in aluminum single crystals by boron treatment in solid state

Rimma Lapovok^{1,2,*} , Yaron Amouyal¹ , Yuanshen Qi¹ , Alex Berner¹ , Anna Kosinova¹ , Eugene Lakin¹ , Dmitri A. Molodov³ , and Emil Zolotoyabko¹ 

¹Department of Materials Science and Engineering, Technion - Israel Institute of Technology, Haifa 32000, Israel

²Institute for Frontier Materials, Deakin University, Geelong, VIC 3220, Australia

³Institute for Physical Metallurgy and Metal Physics, RWTH Aachen University, Aachen, Germany

Received: 14 May 2019

Accepted: 23 September 2019

Published online:

1 October 2019

© Springer Science+Business Media, LLC, part of Springer Nature 2019

ABSTRACT

Electrical conductivity/resistivity of elemental fcc metals, such as Al and Cu, has been investigated intensively for decades, both theoretically and experimentally. Since these metals are of great practical importance for electrical wiring, reducing their resistivity even by a few percent may have very strong impact on their application effectiveness. In this paper, we report on electrical resistivity measurements in Al single crystals grown by the Bridgman method. We found that their resistivity at room temperature decreases by 11.5% upon heat treatment in a boron environment at 600 °C, i.e., well below the melting temperature of Al ($T_m = 660$ °C). The residual resistivity indeed reaches its lower limit dictated by electron–phonon interaction at room temperature. We explain this effect by the boron-induced formation of distorted regions at the surface of the Al crystals. These regions are 30–50 μm in size and comprise finer grains with an average size of 5 μm , separated by low-angle grain boundaries. Resistivity reduction is mainly due to the getter effect, i.e., the removal of the impurity atoms from the crystal bulk by the outward diffusion to the distorted surface regions.

Introduction

Due to their enormous practical importance, electrical properties of Al and Al alloys have been vastly investigated (see e.g., reviews and books [1–3]). In general, metal resistivity originates in the scattering of electron waves by phonons and different lattice defects: point defects (vacancies, self-interstitials and

atomic impurities), linear defects (dislocation lines and dislocation loops) and planar defects (stacking faults, grain boundaries (GBs) and crystal surfaces). For crystals of macroscopic length, such as those employed in the current study, scattering by external surfaces is negligible. In Al alloys, specific volume defects, such as Guinier–Preston zones and

Address correspondence to E-mail: r.lapovok@deakin.edu.au

intermetallic precipitates [3, 4], can also influence electrical resistivity significantly.

Scattering by phonons cannot be eliminated, but its contribution to electrical resistivity, ρ_{ph} , strongly depends on the absolute temperature, T , as $\rho_{ph} \sim T^5$ well below the Debye temperature, θ_D , and as $\rho_{ph} \sim T$ above θ_D [5]. At room temperature, detailed calculations with $\theta_D = 400$ K provide a $\rho_{ph} = 2.666 \mu\Omega \text{ cm}$ [1], which is very close to the well-established experimental value, $\rho_{ph} = 2.65 \mu\Omega \text{ cm}$ [6].

If defect concentrations are not very high, their contribution, ρ_d , to the total electrical resistivity, ρ , according to the Matthiessen’s rule [3, 5], is simply added to the phonon component, ρ_{ph} :

$$\rho = \rho_{ph} + \rho_d \tag{1}$$

In turn, for rather low-defect concentrations, their partial contributions, ρ_{dj} , can also be counted up:

$$\rho_d = \sum_j \rho_{dj} \tag{2}$$

where the index $j = 1, 2, 3 \dots$ indicates different kinds of defects. Relationship (2) stems from the Nordheim rule [7], established for solid solutions with low concentrations of solute atoms. Comprehensive studies of particular contributions of different types of defects to the electrical resistivity of Al are summarized in [1–3], and for the sake of convenience are given in Table 1.

Therefore, diminishing electrical resistivity at room temperature necessitates reducing the concentration of *randomly* distributed defects. In Al alloys, some increase in electrical conductivity is achieved by partial purification of the Al matrix from Mg and Si solute atoms [4]. Recently, a new approach to enhance both the strength and electrical conductivity by grain refinement down to the sub-micrometer scale was suggested. This approach uses severe plastic deformation of Al–Mg–Si alloys combined with dynamic aging at elevated temperatures [4]. Severe plastic deformation was also applied to

manipulate the microstructure evolution and electrical conductivity in Al–Mn–Si alloys [8, 9].

Other methods, to achieve the same objective, have been developed for pure Al. One of them is refining the melting zone, which together with impurity segregation, leads to high-purity Al [10, 11]. Another method includes boron additions to the Al melt [12, 13]. The role of boron is to bind Ti and some other impurities in the form of intermetallic compounds, such as TiB_2 , thereby substantially reducing the impurity contribution to the electrical resistivity of Al.

In the current research, we apply heat treatments to Al crystals in a boron environment at $T = 600 \text{ }^\circ\text{C}$, i.e., well below the melting temperature, $T_m = 660 \text{ }^\circ\text{C}$, of Al. We show that this method allows us to substantially reduce the electrical resistivity of Al crystals down to the lowest magnitude dictated by electron-phonon interactions.

Experimental details

Materials

An Al single crystal was grown by the Bridgman method in a graphite mold using commercially pure aluminum (99.998%). Crystallographic orientations of the crystal seed and, thereafter, of the grown single crystal were determined by X-ray diffraction (Laue technique) [14].

All experiments described below were carried out with the plate-shaped samples, $25 \times 9 \times 3 \text{ mm}^3$ in size. The samples were fabricated from the grown single crystal by electrical discharge cut. In the produced plates, the $[1\bar{1}0]$ crystallographic direction was along the plate thickness (see Fig. 1). The misalignments between the $[1\bar{1}0]$ direction and the normal to the sample surface were less than 1° .

Heat treatment in a boron environment was performed by embedding the samples in boron powder

Table 1 Contribution of different types of lattice defects to electrical resistivity of Al [1–3]

Defect’s type	ρ_j
Vacancies	$2.2 \mu\Omega \text{ cm} \times \text{concentration, } n_v \text{ (in at.\%)}$
Impurity atoms (in average)	$4.0 \mu\Omega \text{ cm} \times \text{concentration, } n_i \text{ (in at.\%)}$
Dislocation lines	$1.0 \times 10^{-12} \mu\Omega \text{ cm}^3 \times \text{density, } n_l \text{ (cm}^{-2}\text{)}$
Grain boundaries (GB)	$1.4 \times 10^{-6} \mu\Omega \text{ cm}^2 \times \text{“density” (cm}^2\text{/cm}^3\text{)}$
Stacking faults	$4 \times 10^{-7} \mu\Omega \text{ cm}^2 \times \text{“density” (cm}^2\text{/cm}^3\text{)}$

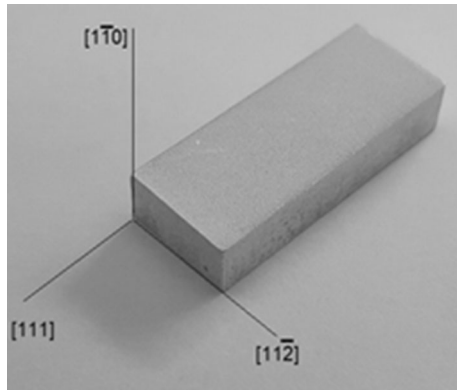


Figure 1 Single-crystal Al sample cut along the indicated crystallographic directions.

(particle size of 1–3 μm). This assembly was encapsulated within a high Cr-content double-walled stainless steel bag to promote remnant oxygen binding. After air evacuation by argon flow, the bag was sealed using resistant spot welding. A detailed description of the solid-state boronizing technique, including interaction between the powder and metal interface, is given in [15]. The entire package was placed in the middle of a cylindrical vacuum furnace, an Electrotherm-16888, close to a thermocouple and heated up to 600 ± 10 °C after reaching vacuum of 2×10^{-5} mbar. The samples were kept at this temperature for 48 h and then cooled down to room temperature, maintaining the vacuum level in the furnace prior to their removal from the stainless steel bag. The duration of heat treatment was selected using the documented diffusion rates of boron in Al [16]. For comparison, similar heat treatments were applied to other Al samples, but with no boron.

Electrical measurements

Electrical resistivity measurements in all investigated samples (pristine and heat-treated, with and without boron) were conducted at room temperature using a *Nemesis*[®] SBA-458 apparatus (Netzsch GmbH, Selb, Germany), which provides instrumental accuracy of individual measurements of about $\pm 5\%$ (based on the four-point eddy current method). To improve the measurement statistics, each measurement was repeated 6–8 times. In these experiments, sharp electrode pins were attached to the $[1\bar{1}0]$ -oriented crystal surface. The electrical resistivity was extracted from the raw U – V curves, which were obtained by varying the current in the range of -0.5 through

$+0.5$ A. Further details about the electrical measurement procedure are found in [17–20].

High-resolution X-ray diffraction (HRXRD)

HRXRD was used to monitor the quality of the Al single crystals and their changes upon heat treatment, for phase analysis, and for tracking the diffuse scattering components. The latter are sensitive to phonons and provide important information about static lattice defects. HRXRD measurements were carried out in the Bragg scattering geometry using a Rigaku SmartLab diffractometry system. The latter is equipped with a 9 kW rotating anode (Cu) generator operating at 45 kV and 200 mA. The instrument has advanced optics for appropriate shaping of the incident and diffracted X-ray beams. In this study, we utilized parallel beam optics of the incident beam, which includes a parabolic mirror, a β -filter, a 5° Soller collimator and a 1-mm-wide incident beam slit. For X-ray registration, a position-sensitive one-dimensional detector D/teX Ultra 250 with 250 strip channels, 75 μm wide each, was used. This detector allowed us to drastically increase the counting statistics and thus to conduct accurate measurements of X-ray diffraction profiles.

Time-of-flight secondary ion mass spectrometry (TOF-SIMS)

Depth distributions of the impurity atoms (including boron) in Al crystals were measured using a TOF-SIMS 5 spectrometer (IONTOF GmbH, Germany), installed in the Technion's Solid State Institute's Surface Science Laboratory. The positive ion depth profiles were taken in a dual mode utilizing 25 keV Bi^+ analysis ions and 1 keV O_2^+ sputtering ions (incident at 45° to the surface for both guns). The data were collected from a $100 \times 100 \mu\text{m}^2$ acquisition area, while the sputtered area was $500 \times 500 \mu\text{m}^2$.

Scanning electron microscopy (SEM)

Modifications of surface morphology, induced by the high-temperature boron treatment, were studied using a Quanta 200 SEM instrument (FEI, USA), equipped with an INCA energy-dispersive spectrometer (EDS) and wavelength-dispersive spectrometer (WDS) (Oxford Instruments, England).

Images were acquired by the backscatter and secondary electron detectors.

Average amounts of impurity atoms, detected by TOF-SIMS, were quantified by WDS. Note also that EDS was insensitive to low impurity concentrations in our samples. Successful WDS measurements were carried out at the optimal working distance of 11 mm, using an accelerating voltage of 30 kV and a probe current of about 40 nA. The takeoff angle of the emitted X-ray fluorescent radiation was 30°. The estimated size of the probed volume is 6–8 μm . The average contents of the different elements were determined by electron probe scanning over an area of $200 \times 200 \mu\text{m}^2$. In addition, in the regions of interest, the concentrations of minor elements were detected using the spot measurement mode. For each region, 10–20 measurements were performed, with the acquisition time being 20 s per single measurement. The analytical lines and standards used for these measurements are listed in Table 2. Quantitative analysis was accomplished applying a conventional ZAF correction procedure. We were unable to measure the hydrogen, lithium and boron contents because of the low energy of the respective characteristic X-ray lines.

Possible formation of borides upon heat treatment was studied by a field-emission gun high-resolution Zeiss Ultra Plus microscope (HR SEM). Chemical analysis of the inclusions observed in the aluminum matrix, as well as boron concentration analysis within the matrix, was performed by EDS. For this purpose, an X-Max silicon drifted detector (energy resolution of 127 eV and active area of 80 mm^2) attached to the HR SEM was utilized. Quantitative analysis was carried out using electron energy of 3 keV, with B $K\alpha$ and Al $K\alpha$ analytical lines. Acquisition time was 50 s per single measurement.

Selected samples were subjected to electron backscatter diffraction (EBSD) analysis to trace angular misorientations related to low-angle GBs. EBSD measurements were performed using a Bruker

QUANTAX EBSD system attached to the HR SEM (Zeiss Ultra Plus). In these measurements, the energy of the primary electrons was chosen to be 20 keV.

Transmission electron microscopy (TEM)

TEM was applied to visualize lattice defects, such as dislocations and GBs, as well to follow grain formation upon boron treatment. TEM samples were prepared by applying the focused-ion beam (FIB) lift-out technique within an FEI Helios Nanolab Dual Beam G3 microscope. The FEI Tecnai T20 TEM instrument, operating at 200 kV, was used to obtain two-beam bright-field (BF) images and weak-beam dark-field (WBDF) images. The thickness of the TEM lamella was determined using a log ratio (relative) method applied to the low-loss spectrum obtained by electron energy loss spectroscopy (EELS) acquisition. EELS measurements were carried out using an FEI Themis G2 80–300, operating at 300 kV and equipped with a Gatan GIF EELS system.

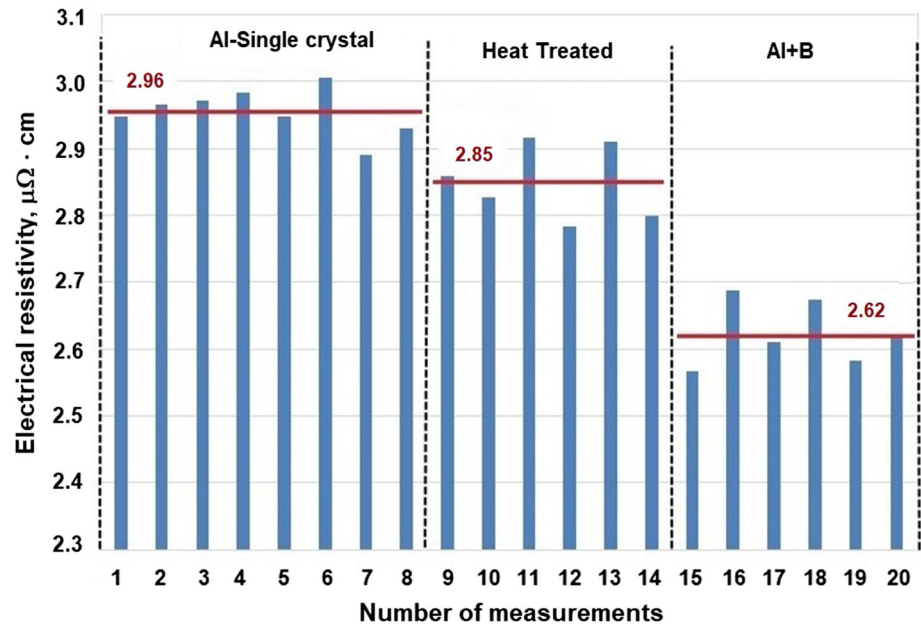
Experimental results and discussion

The results of the resistivity measurements are summarized in the form of a histogram in Fig. 2. For the as-grown (pristine) Al crystals, the average resistivity value was found to be $\rho_0 = (2.96 \pm 0.03) \mu\Omega \text{ cm}$. After annealing at 600 °C without boron, the resistivity decreased slightly by 3.7% to $\rho_a = (2.85 \pm 0.06) \mu\Omega \text{ cm}$. Substantial reduction in the resistivity down to $\rho_B = (2.62 \pm 0.05) \mu\Omega \text{ cm}$, i.e., by 11.5%, however, was observed after heat treatment at 600 °C in the boron environment. Based on the obtained results, we can conclude that (1) heat treatment in a boron environment is, indeed, crucial for resistivity reduction; (2) after this heat treatment, the resistivity value (within the error bars) equals that defined by phonon scattering at room temperature, that is, $\rho_{\text{ph}} = 2.65 \mu\Omega \text{ cm}$ [6]. Furthermore, according to Eq. (1), the resistivity difference (before and after boron treatment), $\Delta\rho = \rho_0 - \rho_B = 0.34 \mu\Omega \text{ cm}$, reflects the defect contribution, ρ_d . In the framework of this research, we applied a set of advanced characterization methods to understand: (1) which kinds of defects are responsible for the increased resistivity in the pristine samples; and (2) what happens to these defects during heat treatment in a boron environment.

Table 2 Analytical lines and standards used for WDS

Element	Line	Standard
Na	$K\alpha$	Egyrin
Mg	$K\alpha$	Diopside
K	$K\alpha$	Orthoclase
Ca	$K\alpha$	Diopside
Cu	$K\alpha$	Pure Cu

Figure 2 Summary of the electrical resistivity measurements. Left-hand part—pristine samples; central part—heat-treated samples with no boron; right-hand part—heat-treated samples in boron environment. Red horizontal lines represent average resistivity values.

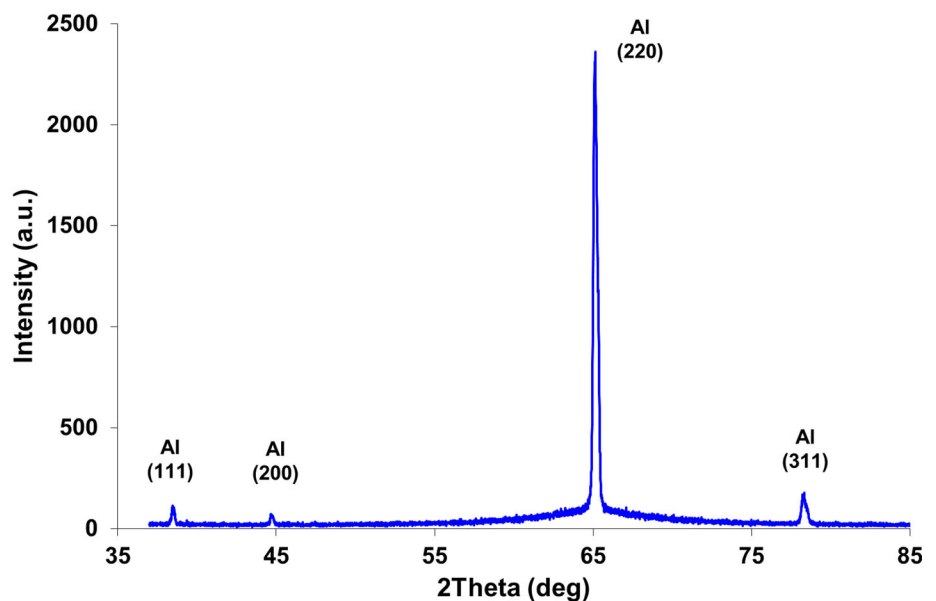


Origin of extra resistivity in pristine Al crystals

The overall structural quality of the Al crystals was inspected by HRXRD. A typical diffraction profile, taken from one of the as-grown crystals with parallel X-ray beam in the Bragg scattering geometry, is shown in Fig. 3. Note that in these measurements, the X-rays entered the crystal through the $[1\bar{1}0]$ -oriented surface. The crystal was intentionally placed slightly off the exact alignment in order to considerably suppress a very intense (220) single-crystal

diffraction peak and, hence, to resolve finer diffraction features. As expected, the (220)-reflection at $2\theta_B = 65.1^\circ$ is still the strongest one; however, additional tiny peaks, such as (111), (200) and (311), are also visible. This means that pristine single crystals are not 100% perfect; there exist some crystalline regions in which not the $(1\bar{1}0)$ -planes, but the (111)-, (100)- or (311)-planes are parallel to the largest crystal surface. Most likely, these regions arise during the sample cutting procedure and are situated near the surface of the sample. This conclusion is supported by TEM images, in which we can recognize a few

Figure 3 HRXRD profile ($\theta/2\theta$ -scan) taken with parallel X-ray beam from one of the pristine samples. X-rays are entering through the $[1\bar{1}0]$ -oriented surface.



plasticity-mediated fuzzy boundaries [21], most probably induced by the sample cut (see Fig. 4).

Nevertheless, at this stage, we can exclude GBs from consideration as a potential source of $\Delta\rho$ in our pristine samples, since their contribution to the total resistivity becomes significant for fine-grained polycrystalline materials only, i.e., when grain size, R , is about 100 nm and below. In fact, the “density” of the GBs (total surface/volume ratio, f_{sv}) is $f_{sv} \approx R^{-1}$. Therefore, to provide $\Delta\rho \geq 0.1 \mu\Omega \text{ cm}$ (taking into account data from Table 1), the grain size needs to be smaller than some critical radius, $R_c \approx (1.4 \times 10^{-6} / 0.1) \text{ cm} = 1.4 \times 10^{-5} \text{ cm} = 140 \text{ nm}$. Clearly, our almost perfect pristine crystals do not fit this criterion. Also noteworthy is that TEM observations revealed no stacking faults, so that these planar defects are irrelevant to our analysis as well.

Dislocation lines were not observed in the pristine samples; however, a few of them were detected in TEM micrographs taken from heat-treated (with no boron) samples (see Fig. 5). For dislocation analysis, we used both the two-beam bright-field (TBBF) method and the weak-beam dark-field (WBDF) technique near the reciprocal lattice vector, $g = 220$. Note that the WBDF technique provides a sharper contrast and, hence higher spatial resolution than TBBF [22]. Using the calculated (with the aid of the EELS low-loss spectrum) sample thickness of 200 nm, the dislocation density was estimated to be $n_l = 2.5 \times 10^8 \text{ cm}^{-2}$. Based on the data given in

Table 1, we find the dislocation contribution to electrical resistivity to be equal to $\rho_l = 10^{-12} \times n_l = 2.5 \times 10^{-4} \mu\Omega \text{ cm}$, i.e., three orders of magnitude lower than $\Delta\rho = 0.34 \mu\Omega \text{ cm}$. In other words, dislocation lines are also irrelevant, providing a negligible contribution to the electrical resistivity in our samples.

Summarizing the above-mentioned findings, we conclude that the resistivity of pristine samples is the sum of the *phonon* and *point defect* contributions. In this context, we would like to emphasize another important feature in the collected HRXRD profiles, i.e., broad diffuse scattering around the strongest (220) diffraction peak (see Fig. 3). This diffuse scattering is revealed very clearly on the logarithmic scale of intensity shown in Fig. 6 together with the fit (red curve) to the Lorentzian function:

$$I = \frac{A}{1 + \left(\frac{Q-g}{G}\right)^2} \tag{3}$$

where A is the fitting parameter, G is the Lorentzian width and $q = Q - g$ is the deviation of the scattering vector, Q , from its exact magnitude, g , at the Bragg position. Note that Eq. (3) provides the correct asymptotic behavior, $I \sim \frac{1}{q^2}$, for $q \gg G$, which is the characteristic of both thermal diffuse scattering (by phonons) and specific static diffuse scattering (so-called Huang scattering due to point defects) [23]. Furthermore, the width of the static diffuse scattering is proportional to the defect concentration [23].

Figure 4 Microstructure features in the pristine crystal: **a** bright-field and **b**, **c** dark-field TEM micrographs revealing some fuzzy boundaries near the crystal surface, most probably introduced by the crystal cut procedure.

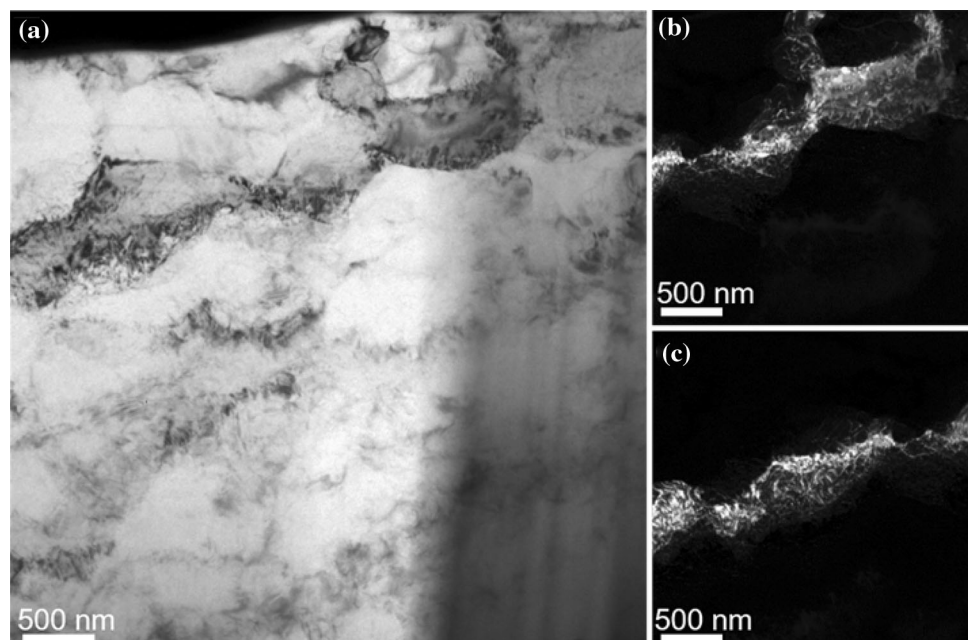


Figure 5 Dislocation lines in the heat-treated (with no boron) crystals: **a, b** Two-beam bright-field images; **c, d** the WBDF images obtained using the diffracting vector, $g = 220$.

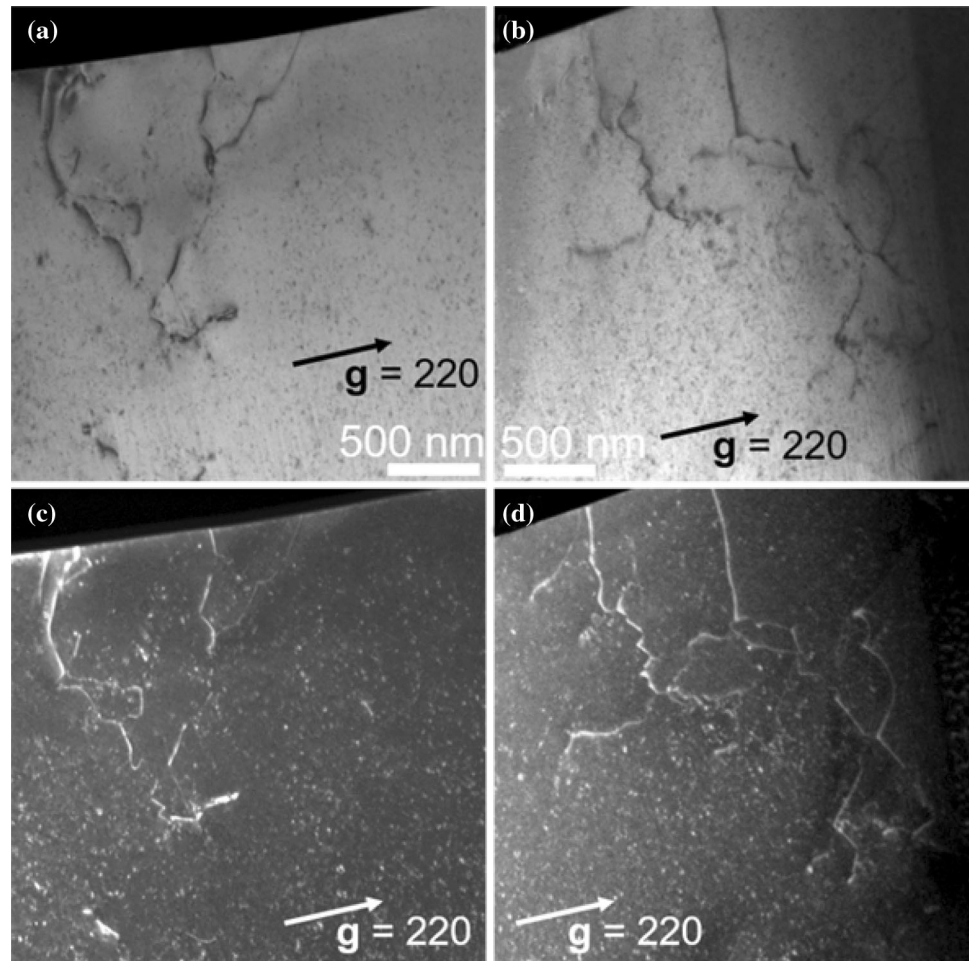
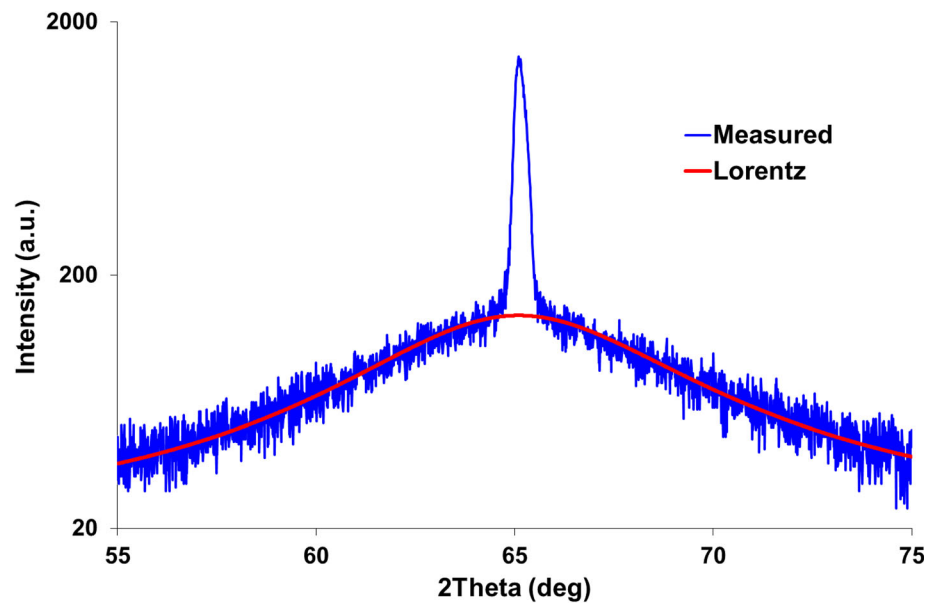


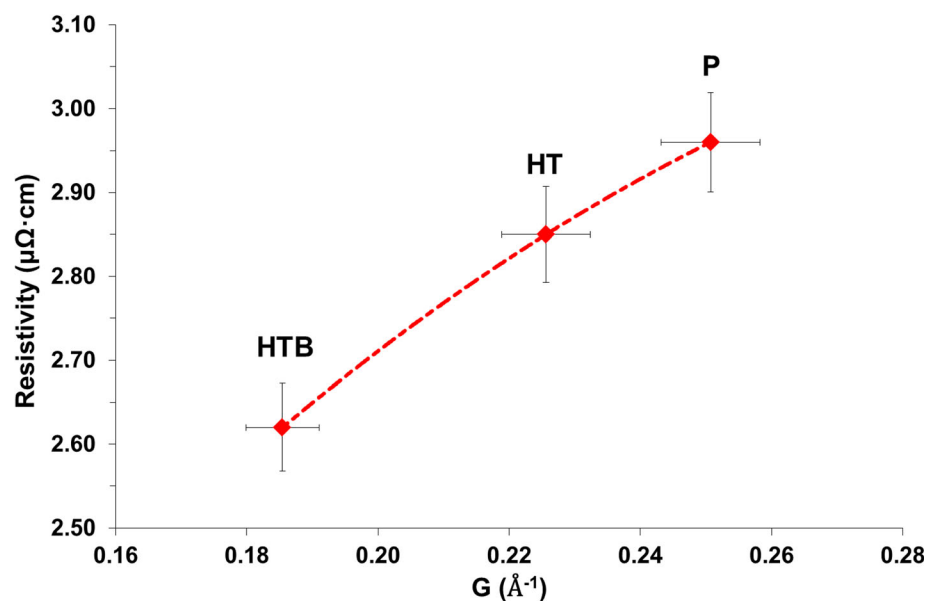
Figure 6 HRXRD profile ($\theta/2\theta$ -scan), taken with parallel X-ray beam from one of the pristine samples in the vicinity of the (220)-reflection ($2\theta_B = 65.1^\circ$). Experimental data are in blue, whereas the Lorentzian fit appears in red.



Bearing this in mind, in Fig. 7, we plot the average resistivity values, obtained in pristine (*P*) samples, heat-treated samples with no boron (HT) and samples heat-treated in a boron environment (HTB), vs. the average Lorentzian width, G , extracted from the respective diffuse scattering profiles. A clear correlation between decreasing resistivity and decreasing Lorentzian width emphasizes the essential role of point defects in determining the resistivity of our Al crystals.

Our next step was to deduce which kinds of point defects contribute to electrical resistivity in pristine samples. We can at once exclude the role of Al vacancies, since their equilibrium concentration at room temperature is negligible, $n_v \approx 10^{-11}$ at.% [24]. Therefore, in our further analyses, we focused on measuring the concentrations of different impurity atoms. Careful measurements of the pristine samples, using WDS in SEM, yielded the following results (summarized in Table 3). We found the presence of at least four different types of impurity atoms, all known to contribute to electrical resistivity. Their total concentration is $\sum_j n_j = 0.074$ at.%. Based on the data given in Table 1, we find that the total contribution of all the impurities to the electrical resistivity equals $0.074 (4 \mu\Omega \text{ cm}) \approx 0.3 \mu\Omega \text{ cm}$. Taking into account that our WDS measurements are not sensitive to light elements, i.e., hydrogen, lithium and boron, we can say that the obtained value fits the measured extra resistivity of pristine samples, $\Delta\rho = 0.34 \mu\Omega \text{ cm}$, well.

Figure 7 Average resistivity values obtained in pristine (*P*), heat-treated with no boron (HT) and with boron (HTB) samples versus average Lorentzian width, G , of diffuse scattering.



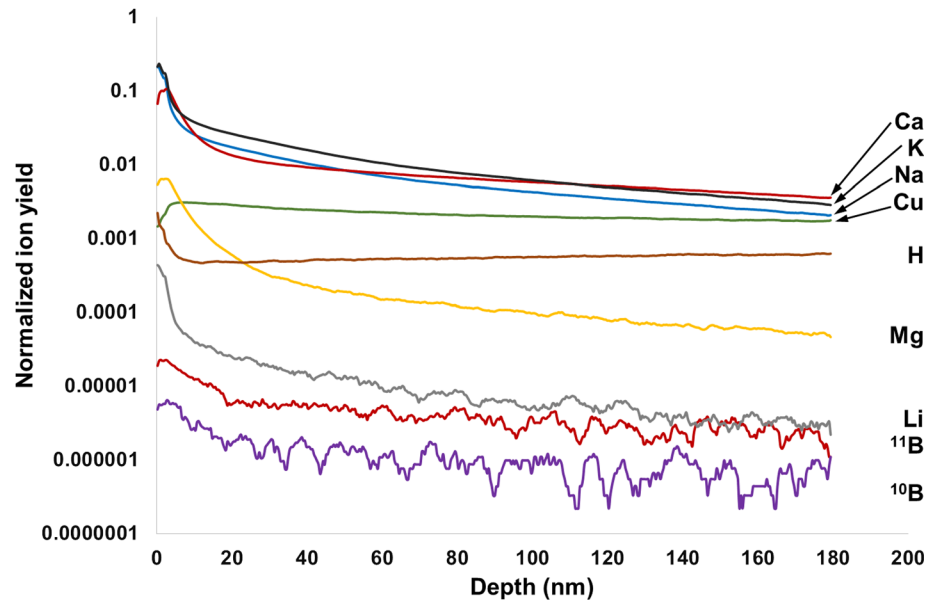
What happens to the impurity atoms during heat treatment in a boron environment?

To answer this question, we first checked the presence of impurities in our samples after heat treatment in the boron environment (HTB samples). To be sensitive to light elements, including boron, we used TOF-SIMS for this purpose. Depth profiles of all detected impurities (normalized to total ion yield over the $100 \times 100 \mu\text{m}^2$ acquisition area) are summarized in Fig. 8. We see that Na, K, Mg, Ca and Cu are present, as well as H, Li and two boron isotopes, B^{11} and B^{10} . Exact quantification of these data is barely possible, but it can be stated that the boron concentration is very low. Application of EDS (at 10 keV) for boron detection failed because of insufficient sensitivity, providing only the upper boron concentration threshold (< 600 ppm). A very rough estimate, based on the comparison with TOF-SIMS signals in the boron-doped Si, suggests that the boron concentration in the interior of the HTB samples is on a ppm level. The latter fits the well-known low boron solubility limit in Al. According to the Al-B phase diagram [25], the maximum boron solubility in solid Al is 45 ppm at the eutectic temperature of 659°C . For higher boron concentrations, aluminum boride, AlB_2 , is formed. These results helped us to understand what happens with boron during heat treatment and what its role is in the resistivity reduction in HTB samples.

Table 3 Concentrations of different impurity atoms (in at.%) measured in pristine samples by WDS in SEM

Element	Average value n_i (at.%)	Detection limit with confident probability of 97.5%
Na	Not detected	0.001
Mg	0.033 ± 0.011	0.025
K	0.0012 ± 0.0005	0.0007
Ca	0.009 ± 0.003	0.0007
Cu	0.030 ± 0.008	0.001
Total	0.074 ± 0.008	

Figure 8 TOF-SIMS results: impurity concentration profiles versus depth in the middle of the sample.



At the beginning of the annealing, boron atoms tend to be dissolved in the Al crystals, but this process is accompanied by a strain/stress accumulation. In fact, large deformation fields arise around both boron substitutional and interstitial defects. In the former case, because the ionic radius of boron is much smaller than that of Al ion; in the latter case, because of the difficulty to swell the close-packed Al crystal lattice locally. For these reasons, near the surfaces of the sample, where the initial boron concentration may be rather high, it is thermodynamically favorable to form AlB_2 particles (see Fig. 9) and in that way to release strain energy.

In fact, such plate-shaped boride particles are visible in the HRSEM images near the sample's borders (see Fig. 9a, b). EDS analysis confirmed that the B/Al atomic ratio within the particles is close to 2:1 (Fig. 9c). A schematic illustration, indicating the location of boride particles within the sample, is shown in Fig. 9d. Furthermore, EDS analysis was performed at an electron energy of 3 keV, so the electron penetration depth into Al is nearly 180 nm.

Therefore, the aluminum boride plates are situated just beneath the irradiated sample surface and are very thin. The latter statement is confirmed by three-dimensional boron distributions measured by TOF-SIMS; a typical example is shown in Fig. 10. Here, we see a boride particle, about $30 \times 10 \mu\text{m}^2$ in the X-Y-plane (Fig. 10a). The depth profile (in the Z-direction) spans over the entire “digging” depth of $Z_d = 200$ nm, but clearly shows diminishing boron concentration, with increasing distance from the particle.

All this (and especially the sketch in Fig. 9d) probably explain why these inclusions are not “visible” in the HRXRD profiles (see Fig. 11). In fact, HRXRD profiles, taken from HTB samples, reveal the Al diffraction peaks only. Nevertheless, it is very intriguing that the intensity distribution between diffraction peaks in the HTB samples is completely different, as compared to that in the pristine samples. In the latter, the (220)-reflection is the strongest one (see Fig. 3), as expected for a single crystal irradiated by X-rays from the $[1\bar{1}0]$ -oriented surface. In contrast,

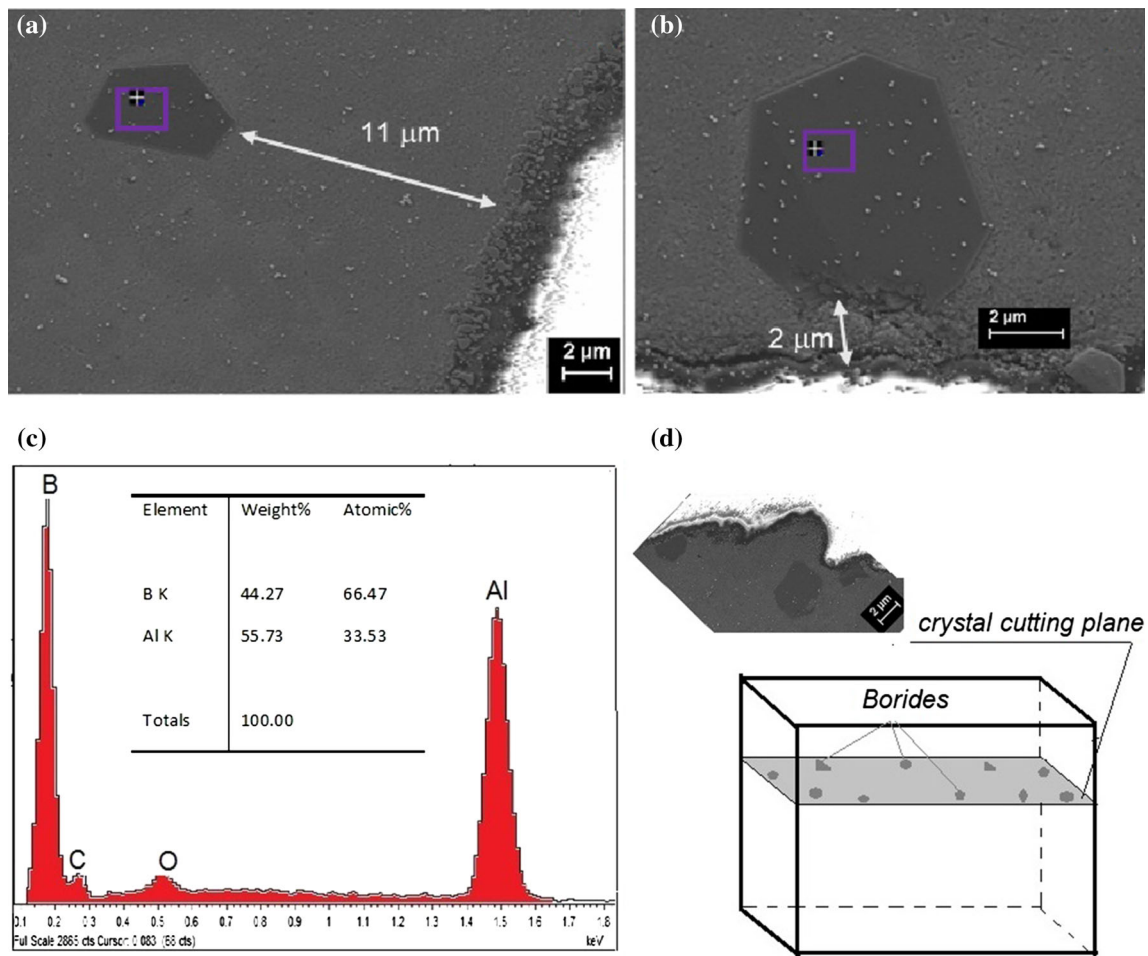


Figure 9 High-resolution SEM images, (a) and (b), of AlB_2 particles located near the surfaces of HTB sample. EDS analysis (c) confirms that B/Al ratio is 2:1. Schematic illustration of the sample cut for these measurements is shown in (d).

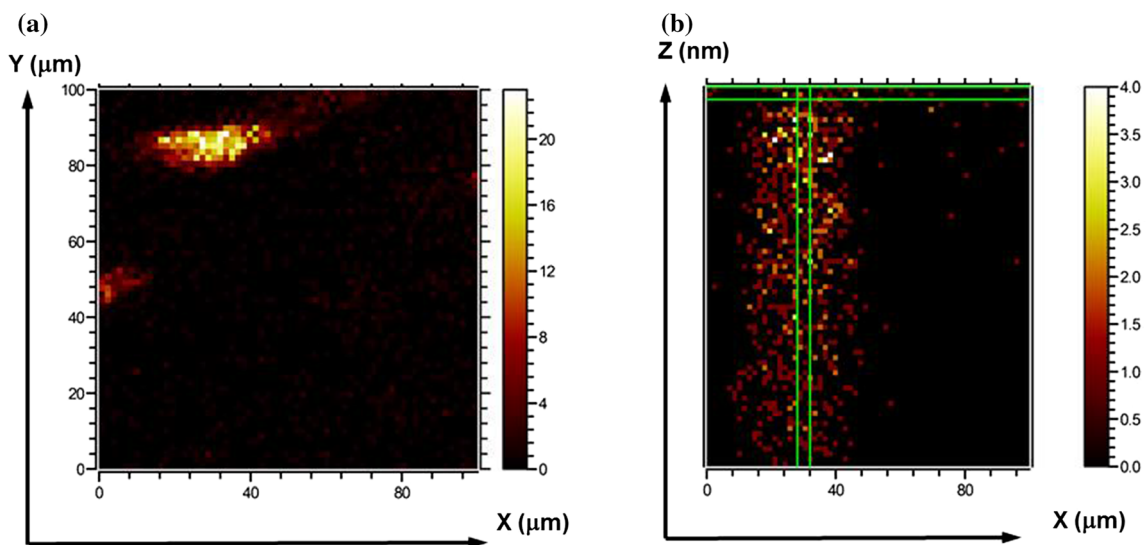
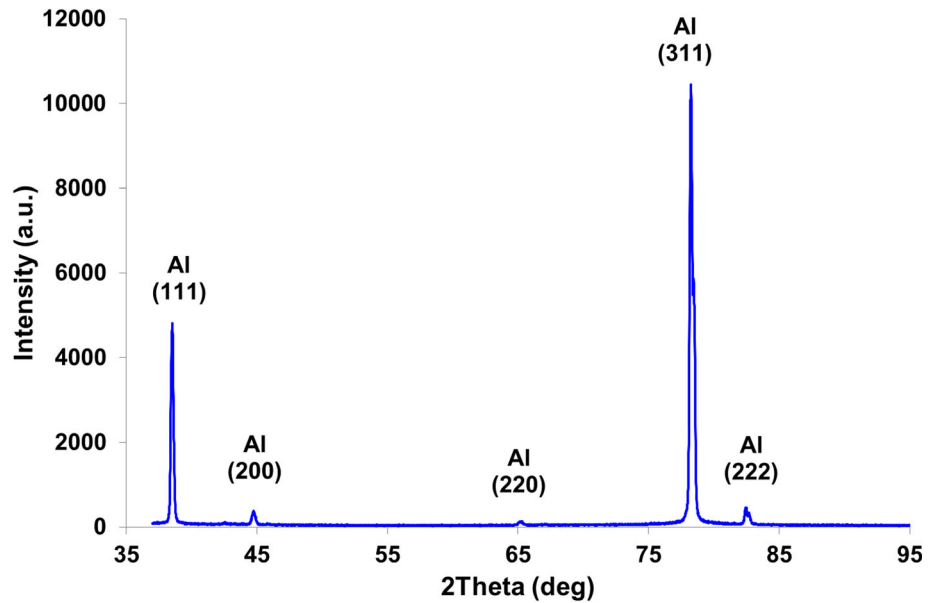


Figure 10 Three-dimensional boron distribution near one of the AlB_2 particles: **a** (X–Y) distribution within a $100 \times 100 \mu m^2$ investigated area; **b** (X–Z) distribution, showing diminishing boron concentration within probed depth, $Z_d = 200 \text{ nm}$.

Figure 11 HRXRD profile ($\theta/2\theta$ -scan) taken with parallel X-ray beam from one of the HTB samples after heat treatment in the boron environment. X-rays are entering through the $[1\bar{1}0]$ -oriented surface.



in the HTB sample, irradiated from the same surface, the strongest one is the (311)-reflection; the next one is the (111)-reflection, whereas the (220) diffraction peak is almost invisible (Fig. 11). This intensity redistribution implies that the HTB samples are no longer entirely single crystalline, but develop (at least close to the surface) a microstructure with differently oriented crystal regions. These distorted regions are clearly visible in SEM micrographs (see Fig. 12) and are 30–50 μm in size. It may be that the most prominent features in these regions are topographic boundaries, about 5 μm in height, which are clearly revealed by SEM images taken with secondary

electrons from 70° tilted surfaces of the HTB samples (see Fig. 13).

TEM measurements showed much finer microstructural features which we call grains. In bright-field (BF) images, the grain structure is clearly resolved, revealing grains of about 5 μm in size, separated by sharp GBs (see Fig. 14). Additional information comes from EBSD measurements carried out with HTB samples (see Fig. 15). Note that prior to EBSD investigation, the sample was mirror polished. In Fig. 15a, we present the kernel orientation map, indicating the misorientation spread within a set of points (kernel) of certain size surrounding the point

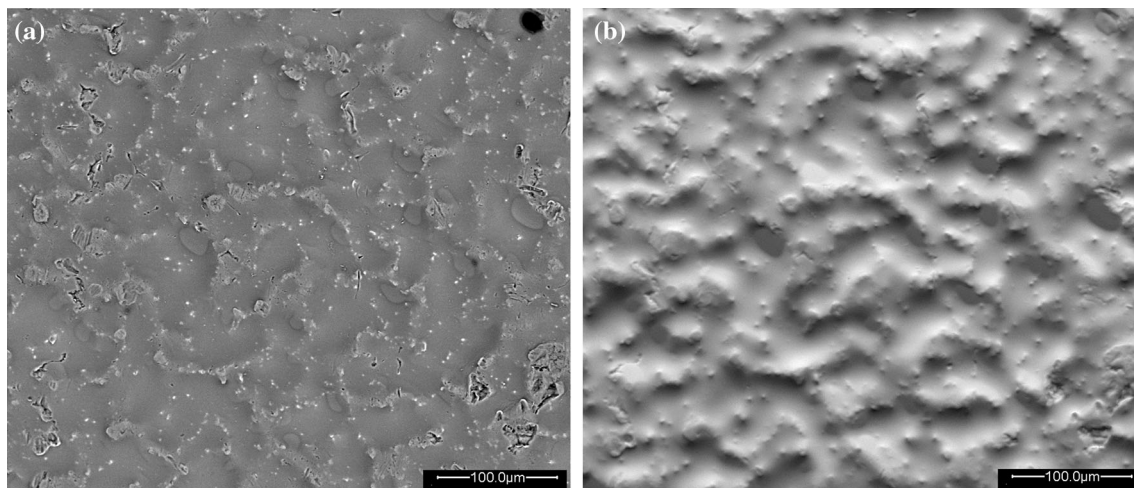


Figure 12 SEM micrographs taken with backscattered electrons from one of the HTB samples in the Z-contrast (a) and topographic contrast (b) modes. Both images show the formation of the distorted regions, 30–50 μm in size.

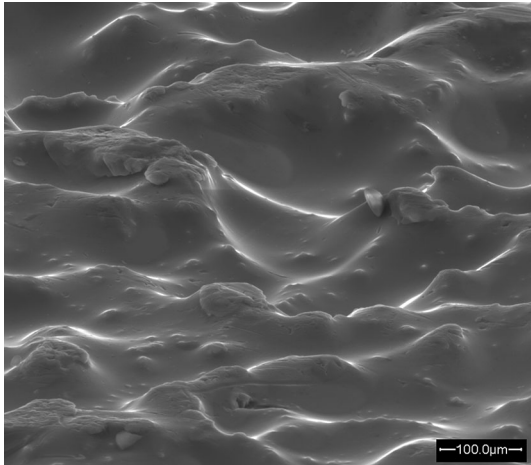


Figure 13 SEM micrograph taken with secondary electrons from a 70° tilted surface of the same sample as in Fig. 12.

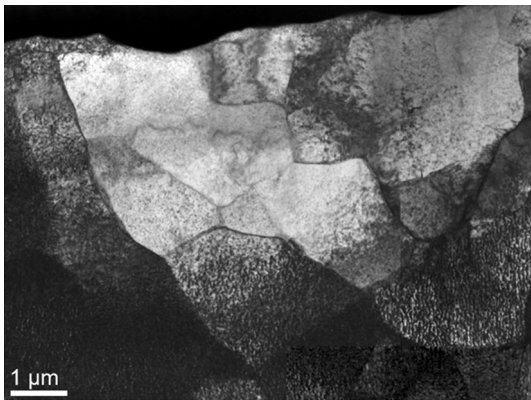


Figure 14 BF-TEM micrograph showing the formation of μm -sized grains in one of the regions visible in Fig. 12.

of interest (see e.g., [26]). We used standard kernel size of 3×3 neighboring points. Quantification of the angular distribution of grain misorientation (Fig. 15b) allows us to conclude that it is dictated by low-angle GBs ($< 15^\circ$). We assume that the development of the grain structure is another way to reduce strain energy in regions where boron concentration is not enough for boride formation. At the same time, the growing “density” of grain boundaries still has a negligible effect on resistivity since a grain size of $5 \mu\text{m}$ is much larger than the above indicated $R_c = 140 \text{ nm}$, below which GBs begin to significantly contribute to Al resistivity.

Topographic features (ridges), outlining the distorted regions visible in Figs. 12 and 13, serve as sinks for impurities, as is revealed by careful WDS measurements. Specifically, we found that despite average impurity concentrations remaining

practically unchanged after boron treatment, in the middle of the distorted regions, atoms of Mg, K and Cu were not detected at all, while the measured Ca concentration was five times smaller than its mean content. In parallel, the concentrations of all measured minor elements at the topographic boundaries were 3–7 times higher than their mean contents.

Based on these results, we assume that upon heat treatment in a boron environment, the majority of impurities exit the crystal bulk, heading toward surface layers heavily distorted by interaction with the boron. This process resembles the well-known getter effect, which is used in Si technology to “clean” undesirable metal impurities from semiconductor devices [27, 28]. To achieve the getter effect, the unused surface regions of the Si wafer are damaged by ion implantation or other methods.

Summary and conclusions

This research focuses on the electrical resistivity changes in Al single crystals upon heat treatment in a boron-rich environment. We found that in pristine samples, the average resistivity is $2.96 \mu\Omega \text{ cm}$, being fully determined by scattering of electron waves by phonons and impurity atoms. Heat treatment for 48 h at 600°C with no boron resulted in a subtle reduction in resistivity down to $2.85 \mu\Omega \text{ cm}$ (by 3.7%) due to partial annealing of point defects. In contrast, the same heat treatment, but in a boron environment, led to drastic resistivity reduction, down to $2.62 \mu\Omega \text{ cm}$ (by 11.5%). The latter value reflects the inevitable phonon contribution at room temperature. To understand the boron effect on resistivity reduction, we applied a set of advanced characterization methods to track the changes in the elemental and phase contents, as well as microstructure modifications. It turned out that because of the low boron solubility in solid aluminum (maximum 45 ppm at 659°C), boron penetration is greatly hampered by the strong deformation fields surrounding the boron impurities. If local boron concentration is high enough, the strain energy is liberated by the formation of AlB_2 inclusions. In regions with lower boron concentration, lattice deformations lead to the formation of distorted surface regions ($30\text{--}50 \mu\text{m}$ in size), delineated by topographic ridges about $5 \mu\text{m}$ high. These regions comprise much smaller grains, nearly $5 \mu\text{m}$ in size, separated by low-angle GBs.

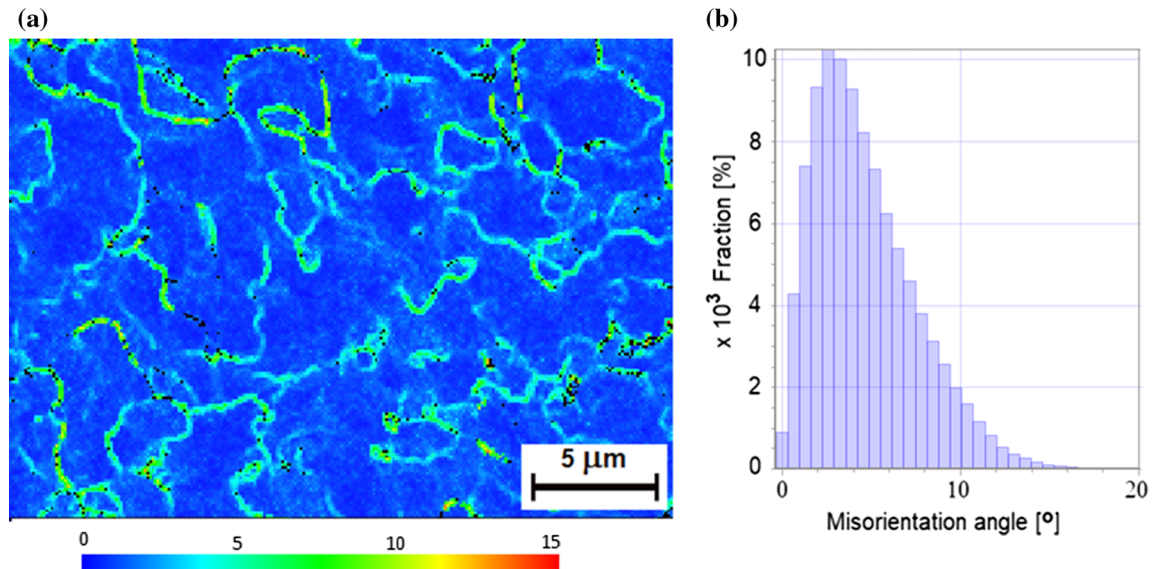


Figure 15 EBSD results obtained in the mirror-polished HTB sample: **a** the kernel misorientation map (the color scale for misorientation angles is in degrees); **b** the distribution of the misorientation angles revealing low-angle GBs.

Development of the described microstructure facilitates impurity segregation to topographic ridges on the sample surface. In this way, the impact of initially randomly distributed impurity atoms on electrical resistivity is greatly suppressed. This phenomenon resembles the getter effect, which is used in silicon technology to clean non-desirable impurity atoms from Si wafers.

Acknowledgements

Prof. R. Lapovok acknowledges the Marie Curie Fellowship within the EU Framework Program for Research and Innovation ‘HORIZON 2020’ (Grant - 742098). We thank Dr. T. Kravchuk for her help with TOF-SIMS measurements.

References

- [1] Fickett FR (1971) Aluminum. A review of resistive mechanisms in aluminum. *Cryogenics* 10:349–366
- [2] Lifshitz BG, Kraposhin VS, Linezky YL (1980) Physical properties of metals and alloys. Metallurgia Press, Moscow, p 319
- [3] Rositter PL (2003) The electrical resistivity of metals and alloys. Cambridge University Press, Cambridge
- [4] Valiev RZ, Murashkin MYu, Sabirov I (2014) A nanostructural design to produce high-strength Al alloys with enhanced electrical conductivity. *Scripta Mater* 76:13–16
- [5] Ziman JM (1979) Principles of the theory of solids. Cambridge University Press, Cambridge
- [6] Gall D (2016) Electron mean free path in elemental metals. *J Appl Phys* 119:085101
- [7] Crystal Growth Technology (2011) From fundamentals and simulation to large-scale production. In: Scheel HJ, Capper P (eds) Wiley-VCH Verlag, p 497
- [8] Pouraliakbar H, Jandaghi MR, Khalaj G (2017) Constrained groove pressing and subsequent annealing of Al–Mn–Si alloy: microstructure evolutions, crystallographic transformations, mechanical properties, electrical conductivity and corrosion resistance. *Mater Des* 124:34–46
- [9] Jandaghi MR, Pouraliakbar H (2018) Elucidating the microscopic origin of electrochemical corrosion and electrical conductivity by lattice response to severe plastic deformation in Al–Mn–Si alloy. *Mater Res Bull* 108:195–206
- [10] Hashimoto E, Ueda Y, Kino T (1995) Purification of ultra-high purity aluminium. *J de Physique IV* 5:153–157
- [11] Ueda Y, Hashimoto E, Tamura H, Kino T (1995) Anisotropy of electrical resistivity in high purity aluminium single crystals. *J de Physique IV* 5:287–292
- [12] Alamdari HD, Dube D, Tessier P (2013) Behavior of boron in molten aluminum and its grain refinement mechanism. *Metal Mater Trans A* 44:388–394
- [13] Marcantonio JA, Mondolfo LF (1971) Grain refinement in aluminum alloyed with titanium and boron. *Metal Trans* 2:465–471
- [14] Molodov DA, Ivanov VA, Gottstein G (2007) Low angle tilt boundary migration coupled to shear deformation. *Acta Mater* 55:1843–1848

- [15] Faran F, Gotman I, Gutmanas EY (2000) Experimental study of the reaction zone at boron nitride ceramic–Ti metal interface. *Mater Sci Eng A* 288:66–74
- [16] David M, Connétable D (2017) Diffusion of interstitials in metallic systems, illustration of a complex study case: aluminum. *J Phys Condens Matter* 29:1361–1368
- [17] de Boor J, Stiewe C, Ziolkowski P, Dasgupta T, Karpinski G, Lenz E, Edler F, Mueller E (2013) High-temperature measurement of Seebeck coefficient and electrical conductivity. *J Electron Mater* 42:1711–1718
- [18] Graff A, Amouyal Y (2016) Effects of lattice defects and niobium doping on thermoelectric properties of calcium manganate compounds for energy harvesting applications. *J Electron Mater* 45:1508–1516
- [19] Sheskin A, Schwarz T, Yu Y, Zhang S, Abdellaoui L, Gault B, Cojocar- Mirédin O, Scheu C, Raabe D, Wuttig M, Amouyal Y (2018) Tailoring thermoelectric transport properties of Ag-alloyed PbTe: effects of microstructure evolution. *ACS Appl Mater Interfaces* 10:38994–39001
- [20] Koresh I, Amouyal Y (2017) *J Eur Ceram Soc* 37:3541–3550
- [21] Hughes DA, Hansen N (2000) Microstructure and strength of nickel at large strains. *Acta Mater* 48:2985–3004
- [22] Cockayne D, Ray I, Whelan M (1969) Investigations of dislocation strain fields using weak beams. *Phil Mag* 20:1265–1270
- [23] Zolotoyabko E (2014) Basic concepts of X-ray diffraction. Wiley-VCH, Weinheim
- [24] Simmons RO, Balluffi RW (1960) Measurements of equilibrium vacancy concentrations in aluminum. *Phys Rev* 117:52–61
- [25] Duschanek H, Rogl P (1994) The Al-B (aluminum-boron) system. *J Phase Equilib* 15:542–552
- [26] Wright SI, Novell MM, Field DP (2011) A review of strain analysis using electron backscatter diffraction. *Microsc Microanal* 17:316–329
- [27] Seidel TE, Meek RL, Cullis AG (1975) Direct comparison of ion-damage gettering and phosphorus-diffusion gettering of Au in Si. *J Appl Phys* 46:600–609
- [28] Kang JS, Schroder DK (1989) Gettering in silicon. *J Appl Phys* 65:2974–2985

Publisher's Note Springer Nature remains neutral with regard to jurisdictional claims in published maps and institutional affiliations.